Diurnal Radiation Cycle Impact on the Pregenesis Environment of Hurricane Karl (2010)

CHRISTOPHER MELHAUSER AND FUQING ZHANG

Department of Meteorology, The Pennsylvania State University, University Park, Pennsylvania

(Manuscript received 9 April 2013, in final form 6 December 2013)

ABSTRACT

Through convection-permitting ensemble and sensitivity experiments, this study examines the impact of the diurnal radiation cycle on the pregenesis environment of Hurricane Karl (2010). It is found that the pregenesis environmental stability and the intensity of deep moist convection can be considerably modulated by the diurnal extremes in radiation. Nighttime destabilization of the local and large-scale environment through radiative cooling may promote deep moist convection and increase the genesis potential, likely enhancing the intensity of the resultant tropical cyclones. Modified longwave and shortwave radiation experiments found tropical cyclone development to be highly sensitive to the periodic cycle of heating and cooling, with suppressed formation in the daytime-only and no-radiation experiments and quicker intensification compared with the control for nighttime-only experiments.

1. Introduction

In the tropics, cloud and water vapor distributions in the troposphere—primarily due to deep moist convection and clear-air subsidence—provide important pathways for solar and terrestrial radiation to modify the transient tropospheric thermodynamic structure. An observational study by Johnson et al. (1996, 1999) using soundings from the western Pacific warm pool confirmed the previously documented dominant cloud layers in the tropics by Malkus (1956): low-level cumulus capped by a trade-inversion stable layer and deep-layer cumulonimbus capped by the tropopause. Johnson et al. (1999) also documented a third dominant cloud type and stable layer: low- to midlevel cumulus congestus with tops near the 0°C melting stable layer. These stable layers can inhibit cloud growth and prevent deep moist convection. Generally, enhanced gradients in relative humidity (RH) from the detrainment of moist convection are found near the base of the stable layer. A recent study by Posselt et al. (2008) using a tropical environment in radiative convective equilibrium successfully modeled the three distinct stable layers.

Mapes and Zuidema (1996) found that dry, stable layers and associated RH gradients at the interface with moist air below provide a layer of anomalous longwave radiative heating and stabilization at the base of the dry layer and a layer of anomalous longwave radiative cooling of the moist layer below. The moist layer below the dry layer emits relatively larger amounts of longwave radiation, heating the base of the dry layer. Pakula and Stephens (2009) examined the cloud distributions in regions of active tropical convection also using a radiative–convective-equilibrium cloud-resolving model. They simulated increased stable layers and produced similar moisture, stability, and cloud structures to those observed by Johnson et al. (1996, 1999). Moreover, radiation influenced stable layers in the vicinity of RH gradients by the same mechanism studied by Mapes and Zuidema (1996). Pakula and Stephens (2009) found convectively active and convectively suppressed phases in simulations using realistic and modified radiative heating profiles in a cloud-resolving radiative equilibrium model. During convectively suppressed phases, clouds were capped at lower levels, supporting the development of lower-level stable layers with associated RH gradients providing additional stabilization.

Many previous studies also examined the impact of radiative processes on the evolution and precipitation patterns of both tropical and midlatitude mesoscale convective systems (MCSs) (Tao et al. 1996; Miller and Frank 1993). Tao et al. (1996) examined the longwave radiation mechanisms of cloud-top cooling and cloud-base heating,

Corresponding author address: Prof. Fuqing Zhang, Department of Meteorology, The Pennsylvania State University, 503 Walker Building, University Park, PA 16801.
E-mail: fzhang@psu.edu

DOI: 10.1175/JAS-D-13-0116.1

© 2014 American Meteorological Society

differential cooling between cloudy and clear regions, and large-scale environmental cooling. They found that for an MCS observed during the Equatorial Mesoscale Experiment (EMEX), large-scale environmental cooling played a dominant role with regard to storm organization and total precipitation. Longwave radiation provided clear-air cooling throughout the troposphere, reducing the temperature and increasing the RH. In the moist tropics, this reduces the impact of entrainment on developing and organizing deep moist convection, allowing condensation to occur more efficiently, similar to findings by Dudhia (1989). Miller and Frank (1993) also found that the domain-wide destabilization caused by radiative processes modifies the evolution of tropical MCSs.

There have been attempts to study the impact of radiation on tropical cyclone development using idealized simulations. Sundqvist (1970) used an axisymmetric balanced primitive-equation model to simulate the development of tropical cyclones and found that the idealized tropical cyclone grew much more rapidly when radiative cooling of clear air[1] only was included, but there was no impact on the final intensity. Hack (1980) used a similar modeling approach, but with prescribed clear-air and cloudy-air radiative heating profiles. It was found that the tropical cyclone growth rate was similar between experiments with and without radiation, but the experiment with radiation started to intensify at an earlier time and had a greater final intensity, which is also confirmed in Craig (1996). However, following a similar approach to Hack (1980), Baik et al. (1990) found the rate of intensification and final storm intensity was not impacted.

The lack of consensus among these aforementioned idealized studies calls for real-data studies to examine the impact of radiation on tropical cyclone genesis, which will be the focus of the current study. An observational study of hurricanes and tropical cyclones by Steranka et al. (1984) found significant diurnal and semidiurnal cloud cycles in observations of satellite derived cloud-top temperatures. Kossin (2002) confirmed the diurnal oscillations and hypothesized that radiative cooling induced subsidence at night in the region of the hurricane canopy reduces the spatial coverage of high cirrus clouds producing the observed reduction in cloud-top heights. Both studies found that the diurnal and semidiurnal cycle impact was more pronounced farther from the core of the tropical cyclone. Using idealized tropical cyclone simulations, Fovell et al. (2010) found a track sensitivity to radiation through a radiative–cloud feedback, driven by differences in hydrometeor species and number concentration distributions generated through microphysical processes. The amount of longwave emission and absorption from the microphysical differences impacted the storm thermodynamics and dynamics, altering the tropical cyclone structure, development, and track.

This study uses Hurricane Karl (2010) as a case study to focus on the impact of the diurnal radiation cycle on the pregenesis environment of a developing tropical cyclone. Hurricane Karl was the eleventh named storm and fifth major hurricane of the 2010 Atlantic hurricane season, reaching tropical storm strength at 1800 UTC 14 September. Genesis forecasts of Karl were challenging, driven by many factors including a lack of organized convection near the center of low pressure and the misalignment of the low- and midlevel circulations. Karl was observed during the Pre-Depression Investigation of Cloud-Systems in the Tropics (PREDICT) field experiment (Montgomery et al. 2012; Davis and Ahijevych 2012). The goal of PREDICT was to obtain extensive pregenesis environmental observations of potential tropical cyclones to better understand why some tropical waves develop into hurricanes while others do not (Montgomery et al. 2012). Davis and Ahijevych (2012, hereafter DA12), profiled the pregenesis environment of Karl and found that the storm was characterized by strong diurnal variations in deep moist convection, with a maximum in the mid- to late morning and a minimum in the late evening; only immediately before genesis did deep moist convection become constant and extensive.

In this study, a convection-permitting numerical simulation is used to examine the effects of radiation on the pregenesis environment of Hurricane Karl. This paper is organized as follows. The model setup and experimental design of the ensemble and sensitivity experiments are described in section 2. The local environment of the observed system, original ensemble, and sensitivity members are detailed in section 3. Results are presented in section 4, followed by discussions and conclusions in section 5.

2. Model setup and experimental design

a. Forecast model

This study uses the nonhydrostatic Advanced Research Weather Research and Forecasting model (ARW), version 3.1.1 (Skamarock et al. 2008), with three domains; the inner domains (D02 and D03) are two-way nested. The horizontal grid spacing and coverage, from coarse to fine, is D01: 40.5 km, 253 × 163; D02: 13.5 km, 364 × 253; and D03: 4.5 km, 601 × 391

[1] Clear air was defined in the study as all grid points where condensation was not taking place; clouds are implicit since cooling only occurred where clouds are not present.

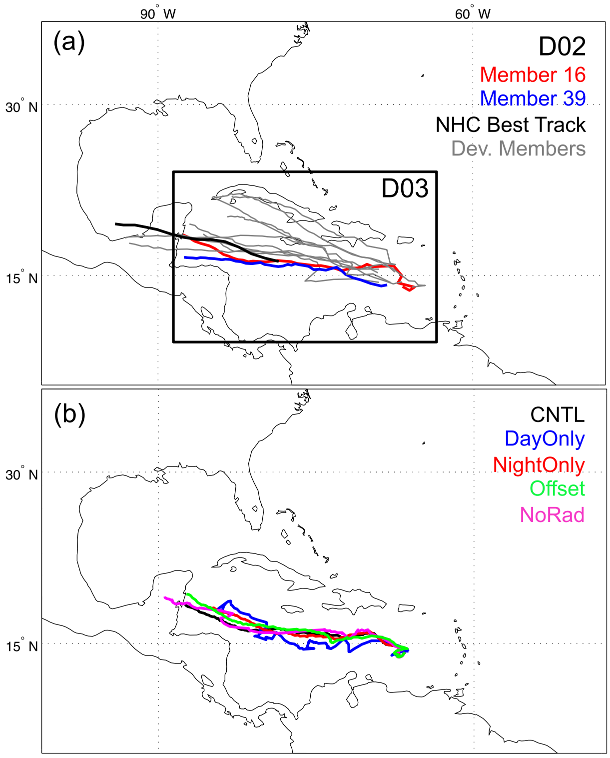

FIG. 1. (a) Model domain setup [outer domain (D01) not shown] for the original ensemble and sensitivity experiment simulations. Overlaid are the vortex-center tracks for developing members for the full original ensemble (Dev. Members; thin gray) with highlighted member 16 (thick red) and member 39 (thick blue) and the NHC best track (thick black). (b) Vortex-center tracks for member-16 sensitivity experiments CNTL (black), DayOnly (blue), NightOnly (red), Offset (green), and NoRad (magenta) plotted in D02. All model simulation tracks are plotted every 3 h for 120 h starting at 0000 UTC 12 Sep. The NHC best track is plotted every 6 h for 78 h starting at 1800 UTC 13 Sep.

(Fig. 1a; D01 not shown). All three domains have 35 vertical terrain following Eta levels and a model top at 10 hPa. Note that the resolution of the model in the lower troposphere, given only 35 total vertical model levels, might not fully resolve the convectively mixed layer and entrainment zone; the entrainment zone is the layer between the convectively mixed layer, herein mixed layer, and the free atmosphere. The WRF single-moment 6-class microphysics scheme (WSM6) (Hong and Lim 2006), Yonsei University (YSU) planetary boundary layer (PBL) scheme (Hong et al. 2006), thermal diffusion surface physics scheme, Rapid Radiation Transfer Model (RRTM) longwave radiative scheme (Mlawer et al. 1997), and Dudhia shortwave (SW) radiation scheme (Dudhia 1989) are employed for all domains. The Grell–Devenyi ensemble cumulus scheme (Grell and Devenyi 2002) is used for D01; no cumulus parameterization is used for D02 and D03. The model domains are two-way nested such that all forecast variables in D03 are directly passed into D02. The use of cumulus parameterization in D02 will make little or no difference owing to the two-way nesting. Nearly all convective activity associated with the development of Karl is within D03. Also, cumulus parameterization was not included in D02 to avoid spurious gradients in water vapor at the boundary of D02 and D03.

The Dudhia shortwave and RRTM longwave radiation schemes and the WSM6 microphysics scheme within WRF interact implicitly. Heating from the radiation schemes modifies the thermodynamics of the environment, impacting cloud processes and vice versa. At any given grid point in a model column, the net heating is a summation of the shortwave and longwave heating from their respective schemes. Each radiation scheme uses the cloud fraction to determine if the scheme is calculating a cloudy or clear-air heating rate. The cloud fraction for the Dudhia and RRTM schemes are determined from the cloud mixing ratio q_c or summation of cloud mixing ratio and ice mixing ratio q_{ci}. If q_c or q_{ci} is greater than the set threshold of $10^{-6}\,\mathrm{kg\,kg^{-1}}$, the cloud fraction is set to 1 and the cloudy heating rates are calculated; otherwise the cloud fraction is set to 0 and clear-air heating rates are calculated. The terms q_c and ice mixing ratio q_i are prognostic variables within the WSM6 microphysics scheme; the other prognostic variables in the scheme are the mixing ratios of water vapor q_v, snow q_s, rain q_r, and graupel q_G. The Dudhia and RRTM schemes are calculated every 30 min while the WSM6 microphysics scheme is calculated every time step for time steps less than 120 s and every 120 s if the model time step is larger.

The Dudhia (1989) shortwave radiation scheme calculates the downward column shortwave clear-air and cloudy-air heating rates, accounting for clear-air scattering, clear-air water vapor absorption, cloudy-air scattering (albedo effects), and cloudy-air absorption; the calculation is dependent on the binary cloud fraction at a specific level in the column. A cloud fraction of 1 (cloudy air) instructs the model to use cloud radiation processes of cloud backscattering (albedo effects) and absorption. Clear-air scattering and water vapor absorption are calculated when the cloud fraction is 0. For cloudy air, the microphysical quantities at each grid point are taken into account through the liquid water path (LWP). The LWP is used to describe optical properties of the cloud because of its availability in WRF and relationship to optical thickness. The LWP is computed in the Dudhia SW scheme in WRF using a density-weighted summation of the weighted cloud mixing ratio (100%), ice mixing ratio (10%), rainwater mixing ratio (5%), snow mixing ratio (2%), and graupel mixing ratio (5%). LWP is subsequently used in combination with the cosine of the zenith angle of the solar irradiance to determine the cloud scattering and absorption, interpolated from tabulated values from Stephens (1978a,b) theoretical results. Stephens (1978a) showed that the details of the drop size distribution within the cloud are of secondary importance to the vertical distribution of liquid water content within the cloud when calculating the SW radiative flux. The effective radius for the various drop size distributions seen in the cloud types defined by Stephens (1978a) are inherently taken into account when determining the relationship between LWP and optical thickness when deriving the SW parameterization. The reader is directed to Stephens (1978a,b) for further details on the theory and parameterization details.

b. Initial and boundary conditions

The initial conditions are generated from the Pennsylvania State University (PSU) limited-area mesoscale ensemble prediction system using a cycling ensemble Kalman filter (EnKF) (Meng and Zhang 2008a,b; Zhang et al. 2009, 2011; Weng and Zhang 2012). The system was used during PREDICT as part of the forecast guidance and assimilated all data used by the National Centers for Environmental Prediction (NCEP), excluding satellite radiances (Montgomery et al. 2012). For further details on the PSU-EnKF system, the reader is directed to Zhang et al. (2009) and Weng and Zhang (2012). The 30-member ensemble used in this study is initialized from the 0000 UTC 12 September posterior of the real-time analysis from the PSU-EnKF used during PREDICT. The model is integrated for 144 h for each ensemble member without any additional data being assimilated. The boundary conditions for D01 are updated every 12 h from the Global Forecast System (GFS) forecast initialized at 0000 UTC 12 September. The WRF three-dimensional variational data assimilation (WRF-3DVAR) system (Barker et al. 2004) is used to perturb the GFS forecast boundary condition tendencies using balanced random perturbations derived using the ‘‘cv3’’ option for the background error statistics. For further details on the boundary condition generation methodology, the reader is directed to Meng and Zhang (2008a).

c. Sensitivity experiment design

To test the effect of the diurnal cycle on storm development, multiple sensitivity simulations are generated to isolate various parts of the diurnal cycle. These experiments include an endless daytime (solar insolation set at local noon: DayOnly), an endless nighttime (no solar insolation: NightOnly), and the disabling of both longwave and shortwave radiation (NoRad). Normal diurnal cycle experiments are also performed with unmodified radiation (CNTL) and with a reversal of the diurnal cycle that shifts the model time (for shortwave radiative forcing only) backward by 12 h (Offset). General conclusions cannot be adequately drawn from only the analysis of the CNTL forecast and the associated vertical radiation profiles; it is necessary to use the various sensitivity experiments to isolate the extremes of the diurnal cycle. Because of computational restrictions, the sensitivity experiments are performed for two developing (member 16 and member 39; subjectively chosen because of their similarity in track to observations) and two nondeveloping (member 11 and member 37) members of the initial PREDICT ensemble.

d. Storm tracking, storm development criteria, and vertical profile radial averages

The prestorm dislocation of the lower- and midlevel circulations associated with Karl made it difficult to define and track the pregenesis vortex center. For this study, a 2D low-pass fast Fourier transform (FFT) filter is used on the 850- and 500-hPa relative vorticity fields to filter wavelengths less than 300 km prior to application of the tracking algorithm. Composite best-track data from PREDICT is used at 0000 UTC 12 September (local time is UTC − 5 h) to constrain the initial search for the maxima of the 850- and 500-hPa relative vorticity fields. The vortex center is set as the average of the locations of the 850- and 500-hPa relative vorticity maxima. Subsequent searches use the location of the prior vortex center as the initial search point.

Vertical profiles of model variables are generated for the local environment[2] by horizontally averaging each model level within a circle of radius 225 km and for the large-scale environment by averaging over an annulus from 300 to 450 km, both using the 850–500-hPa average vortex center. Storm intensity is defined by the maximum 10-m wind speed within 225 km of the vortex center. A simulation is considered developed when the 10-m maximum wind speed is over 18 m s^{-1}. All diagnostic analyses are performed on D03 unless otherwise noted.

3. Evolution of the local environment

a. Hurricane Karl (2010)

A trough over northern South America merged with a westward-moving tropical wave on 8 September to form an area of low pressure east of the Windward Islands (Stewart 2010). Prior to cyclogenesis, the disturbance was characterized by strong diurnal variations in deep moist convection, discernable in Fig. 2e, which is

[2] The local environment here refers to the inner-core area centered on the incipient vortex center.

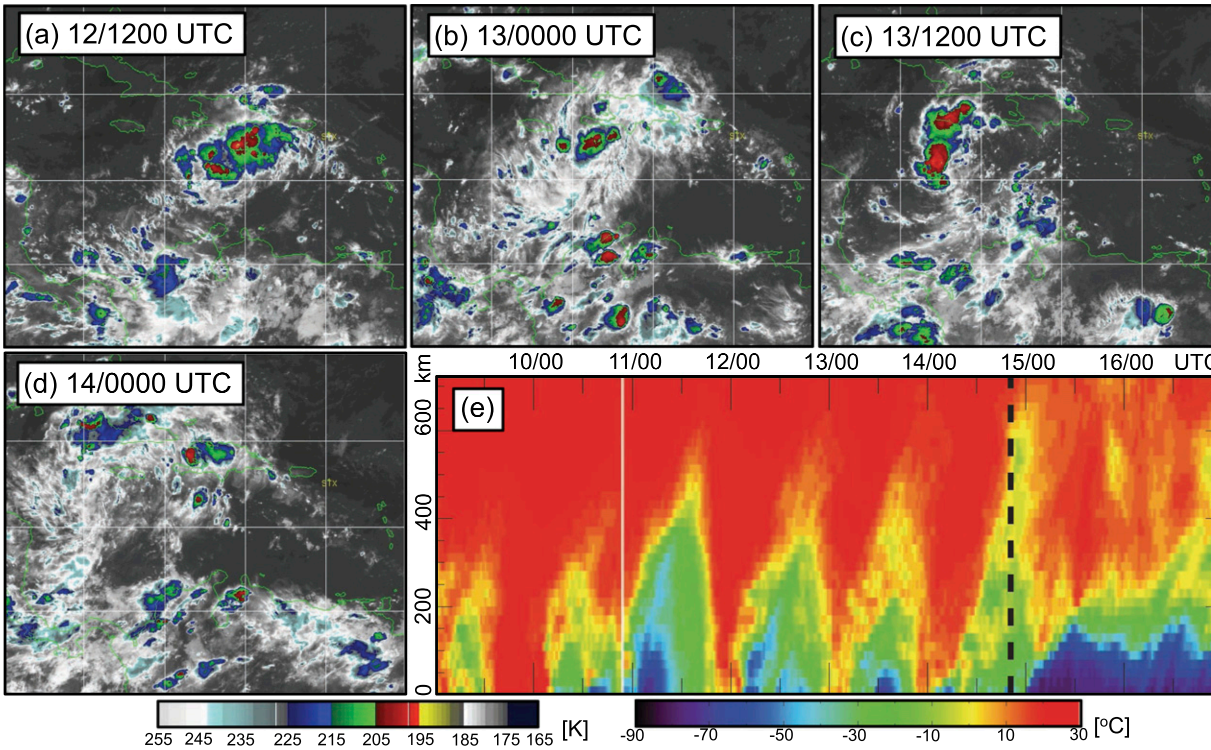

FIG. 2. *GOES-13* channel-4 (~11 μm) enhanced thermal infrared imagery at (a) 1200 UTC 12 Sep, (b) 0000 UTC 13 Sep, (c) 1200 UTC 13 Sep, (d) 0000 UTC 14 Sep, and (e) time–radius diagram of cloud-top temperature (75th-percentile temperature within successive 20-km radial rings) derived from GOES infrared data [adapted from Fig. 3b of Davis and Ahijevich (2012)]. The black dashed line in (e) indicates the time that Karl reached tropical storm status.

a Geostationary Operational Environmental Satellite (GOES) infrared data derived time–radius diagram of cloud-top temperature (adapted from DA12). Pulsations in cloud-top temperature from deep moist convection coincide well with the diurnal cycle: coldest cloud tops near the circulation center around 0600 UTC each cycle, extending radially outward through time with the largest radial extent occurring around 1200 UTC. GOES infrared imagery from 1200 UTC 12 September through 0000 UTC 14 September every 12 h (Figs. 2a–d) depict the spatial distribution of the deep moist convection, the largest concentration of cold cloud tops occurring around 1200 UTC 12 and 13 September to the northwest of the vortex center. DA12 found that the pulsations in deep moist convection helped overcome the negative effects of friction and vertical wind shear produced during the convectively inactive periods. They concluded that deep moist convection and the vertical alignment of the relative vorticity were key environmental factors in the genesis of Karl. Using dropsonde data from PREDICT, DA12 found that in the 4 days prior to genesis, the average environment within 3° of the 900-hPa storm center had RH values between 75% and 80% below 500 hPa, dropping off rapidly to about 40% by 200 hPa (DA12, their Fig. 13b). A large reduction in low-level circulation with a smaller associated reduction in midlevel circulation occurred between 1800 UTC 11 September and 0000 UTC 13 September. The midlevel circulation regained much of its strength by 1200 UTC 13 September, with the low-level circulation (between 900 and 700 hPa) rapidly increasing just prior to genesis on 14 September.

b. *Original ensemble members*

The 30-member ensemble forecasts initialized from the 0000 UTC 12 September cycling PSU-EnKF produced 11 developing and 19 nondeveloping storms. Figure 1a shows the 120-h storm tracks of the developing members and the National Hurricane Center (NHC)'s best track, with the accompanying storm intensity in Fig. 3a. The spread in the intensity exposes the low predictability for the genesis of Karl, with a few members showing immediate genesis and others not until later in the period between 14 and 15 September.

The composite environments of the developing and nondeveloping ensemble members at initialization (0000 UTC 12 September) indicate statistically significant differences in RH, relative vorticity, and deep-layer shear;

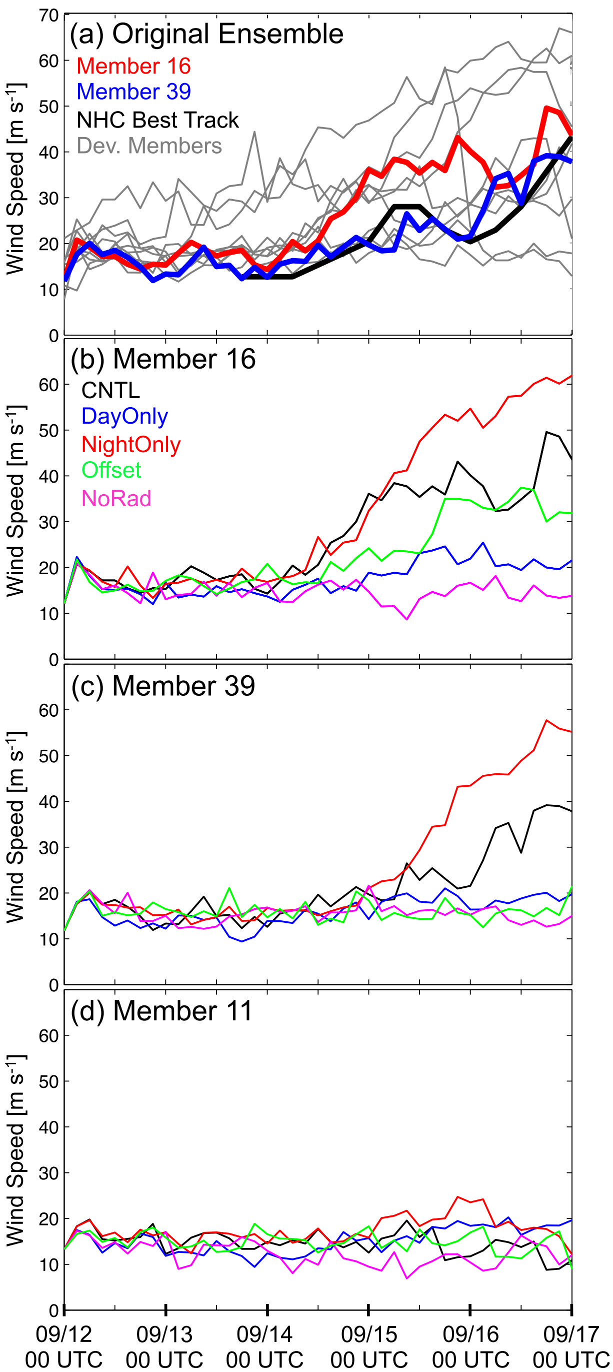

FIG. 3. The evolution of the maximum 10-m wind speeds (m s^{-1}) within 225 km of the average vortex center over the first 120 h of the simulation for (a) the original ensemble, (b) developing member-16, (c) developing member-39, and (d) nondeveloping member-11 sensitivity experiments with CNTL (black), DayOnly (blue), NightOnly (red), Offset (green), and NoRad (magenta). Note that in (a), member-16 CNTL is colored red, member-39 CNTL is colored blue, the NHC best track is thick black, and remaining developed members are light gray; the highlighting scheme is as in Fig. 1a.

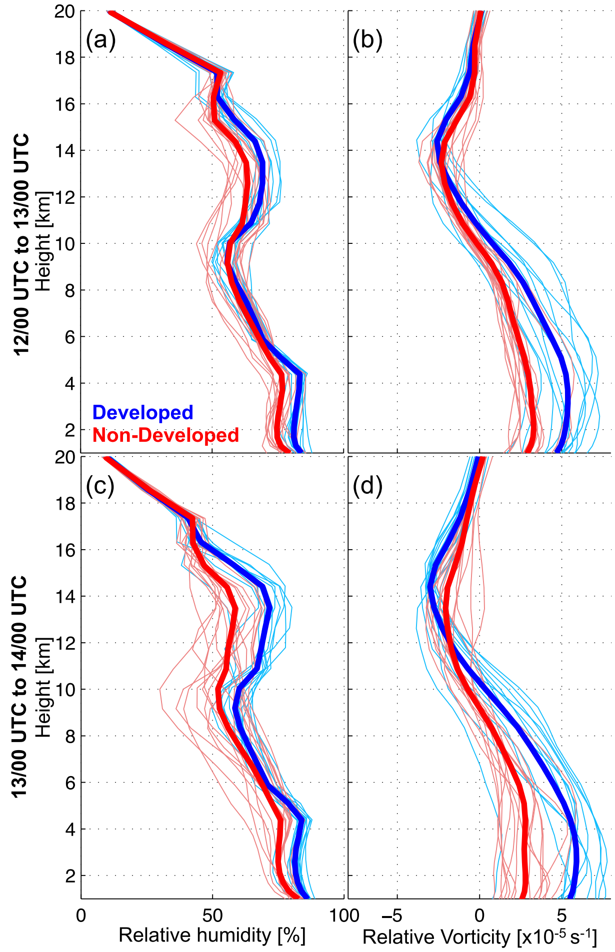

FIG. 4. Vertical profiles of the local-environment (a),(c) relative humidity and (b),(d) relative vorticity averaged within 225 km of the vortex center for each member of the original ensemble over a 24-h period beginning at (top) 0000 UTC 12 Sep and (bottom) 0000 UTC 13 Sep. Developing (nondeveloping) members are colored blue (red), and the mean profile of each group is thick.

these fields, either individually or in aggregate, potentially impact Karl's genesis. The developing members initially have higher 700–500-hPa RH (71.3% versus 65.9%), larger 850-hPa relative vorticity (3.2×10^{-5} versus 2.7×10^{-5} s^{-1}), and stronger 850–200-hPa deep-layer wind shear (8.8 versus 6.4 m s^{-1}) calculated at the vortex center. DA12 found that the displacement of the low- and mid-level circulations was the main contributor to the observed wind shear in Karl, while the background environmental wind shear was a secondary contributor. A large displacement of the vortex centers is observed in the initial conditions generated by the PSU-EnKF system for Karl—a contributor to the observed wind shear.

Figure 4 shows vertical profiles of the local-environment RH (calculated with respect to ice below 0°C) and relative vorticity, averaged over 24 h starting at 0000 UTC

12 September (Figs. 4a,b) and 0000 UTC 13 September (Figs. 4c,d) for developing (blue) and nondeveloping (red) ensemble members. The mean profiles of the developing and nondeveloping ensemble members are thick. Consistent with the past studies of McBride and Zehr (1981), Sippel and Zhang (2008, 2010), Zhang and Sippel (2009), Torn and Cook (2013), Munsell et al. (2013), and Poterjoy and Zhang (2014), during both periods before cyclogenesis, the developing members, on average, have higher RH as well as larger low- to midlevel relative vorticity.

c. Sensitivity experiments

As described in section 2c, the effect of the diurnal cycle on storm development is analyzed by sensitivity experiments that modify the radiation applied to a given simulation in an attempt to isolate the extremes of the diurnal cycle. The impact on the intensification can be seen in Figs. 3b–d with the intensities of two developing members (16 and 39) and one nondeveloping (member 11; member 37 not shown because of the similarity with member 11), spanning 12–17 September. CNTL and NightOnly for members 16 and 39 all develop; the NightOnly simulations are generally more intense compared with the CNTL runs. Member 16's Offset develops while member 39's Offset does not develop, even though both receive the same additional period of solar radiation after initialization. None of the DayOnly and NoRad experiments develop. Some of the nondeveloping sensitivity experiment members attain marginal tropical storm wind speeds but develop broad and less organized convection with weaker low- to midlevel circulation; as such, the maximum wind speed overstates the development of these storms.

It should be noted that the switch from local late evening, when the sun is nearly set, to local noon in the DayOnly experiments at simulation initialization generates no discernible transient response in the initial model fields. The initial fields minimally vary between sensitivity members during the first 6 h; distinguishable differences are not evident until about 10 h. The impact of radiation is an integrated effect, taking time to substantially alter the simulations. Additional tests were performed using initial conditions at 1800 UTC 11 September with the same DayOnly radiative forcing; all exhibit similar behavior (not shown).

All sensitivity experiments' vortex centers throughout the first 24 h are near 15°N latitude, with the tracks staying within $\pm 2°$ latitude as the simulations progress; DayOnly makes the largest deviation of member 16's sensitivity experiments. Within the first 24 h, land-modified air from the tip of South America and islands surrounding the eastern Caribbean Sea minimally interact with the local environment of the circulation. Therefore, the analysis of the pregenesis environment is focused on the first 24 h in order to minimize complications induced by land, including enhanced sea-breeze circulations and overproduced convection due to increased surface heating of land in the DayOnly experiments.

To examine the predevelopment environment and subsequent evolution of the sensitivity experiments for the developing members, the analysis focuses on member 16 for simplicity. Member 39 showed very similar evolution for each sensitivity experiment except for Offset; the nature of this experiment will be discussed in the next section. Unless otherwise noted, the remaining discussion and figures all reference member 16. Vertical profiles of the average local-environment hourly model output from 0000 UTC 12 September to 1200 UTC 15 September of RH (%), cloud-water and ice mixing ratio ($g\,kg^{-1}$), and relative vorticity ($\times 10^{-4}\,s^{-1}$) are shown in Fig. 5 for CNTL, DayOnly, and NightOnly. The cloud water and ice mixing ratios for CNTL and NightOnly (Figs. 5b,h) indicate three local cloud maxima: above the mixed layer of the PBL in the entrainment zone ($\sim$1.5 km), near the 0°C melting level ($\sim$5 km), and below the tropopause ($\sim$12 km). During the first 24 h, CNTL and NightOnly both produce deep moist convection, hypothesized to be a precursor for aiding in the development of a deep vortex later in the simulation, as seen in Zhang and Sippel (2009). DayOnly does not exhibit strong vertical development during the first 24 h.

Focusing on the RH in Figs. 5a, 5d, and 5g, DayOnly has a decrease in RH from 2 km up to the tropopause compared with CNTL and NightOnly, although a weak signal of drier mid- to upper-level air is present in CNTL and NightOnly from 6 to 10 km. In DayOnly, the constant bombardment of shortwave radiation increases the temperature above the boundary layer and entrainment zone (see moist static energy discussion and corresponding Fig. 8), dropping the RH; a pronounced decrease in RH is seen by the end of the first 24 h from 8 to 14 km in DayOnly. The warmed local environment for DayOnly reduces the initial convective burst midday on 12 September that occurs in developing members CNTL, NightOnly and marginally in Offset.

The relative vorticity is similar for CNTL, DayOnly, and NightOnly during the first 12 h, but by 1800 UTC 12 September, CNTL and NightOnly diverge from DayOnly with increased mid- to upper-level relative vorticity (Figs. 5c,i). Increased midlevel relative vorticity is evident in CNTL and NightOnly by 1200 UTC 13 September.

The average 850–500-hPa local-environment relative vorticity for the first 3 days of the simulation is shown in Fig. 6. The strength of NightOnly over CNTL is evident after 0000 UTC 14 September and corroborates that

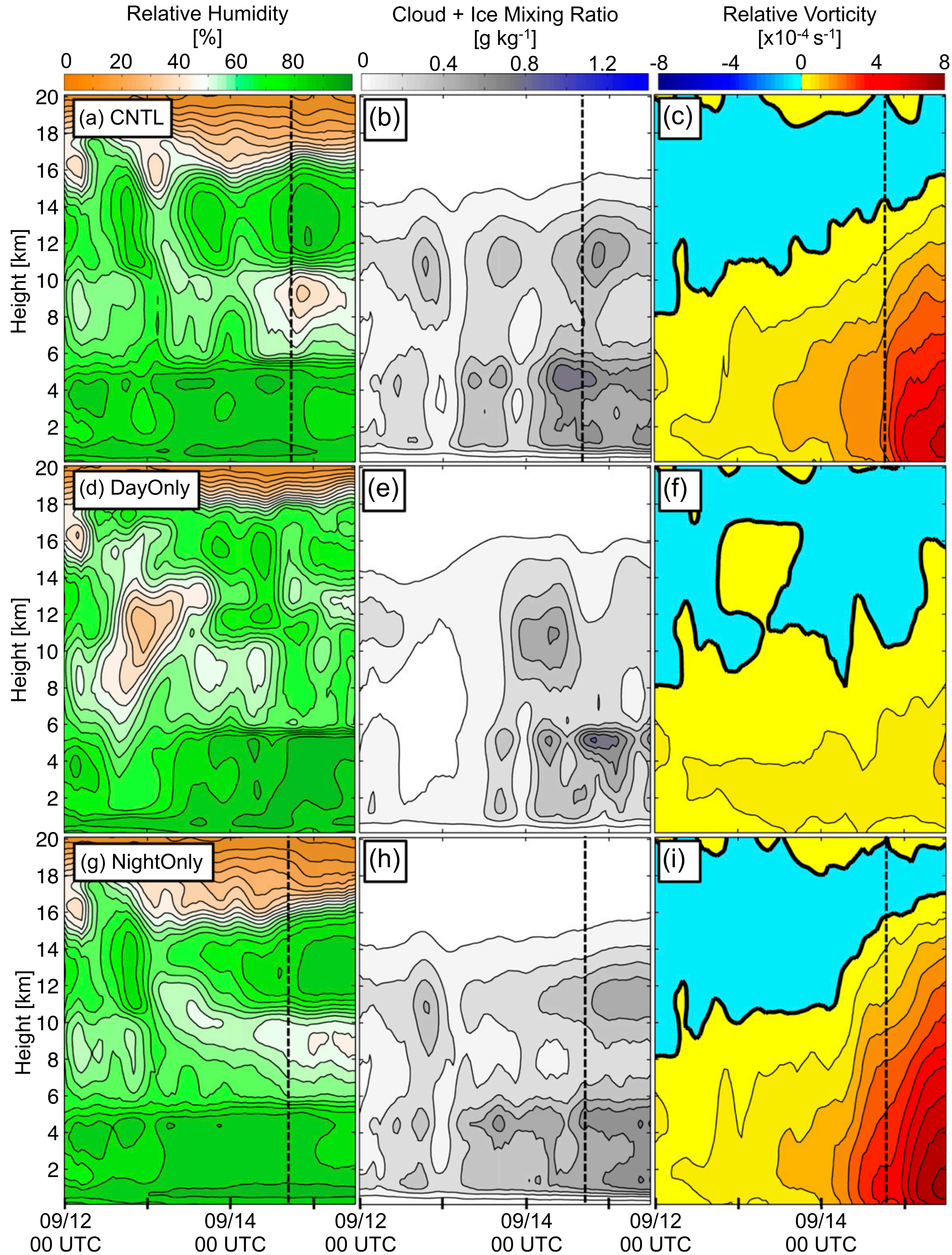

FIG. 5. Vertical profiles of the average local-environment hourly model output within 225 km of the vortex center of (a),(d),(g) relative humidity (shaded every 5%), (b),(e),(h) combined cloud water and ice mixing ratio (starting at 0.05 g kg^{-1}; shaded every 0.15 g kg^{-1}), and (c),(f),(i) relative vorticity (thick black line denotes zero, shaded every 5×10^{-5} s^{-1}) for member-16 sensitivity experiments (top) CNTL, (middle) DayOnly, and (bottom) NightOnly. The black dashed lines indicate genesis time for the corresponding sensitivity experiment.

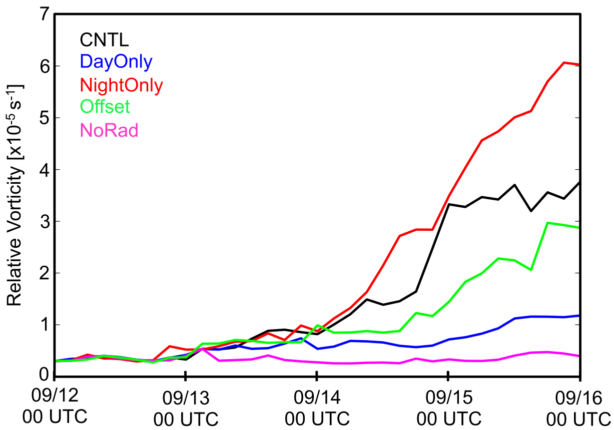

FIG. 6. Temporal evolution of the average 850–500-hPa relative vorticity ($\times 10^{-5}\,s^{-1}$) within a 225-km radius of the vortex center for all member-16 sensitivity experiments CNTL (black), DayOnly (blue), NightOnly (red), Offset (green), and NoRad (magenta).

seen in Figs. 5c and 5i. After 0000 UTC 14 September, NightOnly maintains the largest average magnitude over the other sensitivity experiments. There is a delay in the development and intensification of Offset, lagging NightOnly and CNTL by about 18 h. Once intensification begins, the rate of intensification of NightOnly is the largest, CNTL and Offset are similar, and DayOnly and NoRad do not develop. These results are similar to Sundqvist (1970), who found an increased intensification rate when clear-air cooling was included.

The alignment of the low- and midlevel circulations was found to be instrumental in the genesis of Karl (DA12). The alignment of the low- (850 hPa) and midlevel (500 hPa) relative vorticity is evident in Fig. 7. At 1200 UTC 12 September (Figs. 7a,e,i), all three simulations have similar alignment of low- and midlevel circulations. As the simulation progresses, the strength of both low- and midlevel circulations for DayOnly remains weak and the misalignment is much larger than that of CNTL and NightOnly (Figs. 7c,g,k). By 1200 UTC 14 September, about 3 h before tropical cyclogenesis, CNTL and NightOnly are well aligned with a surface depression evident in the sea level pressure fields and strong low- and midlevel relative vorticity.

An analysis of the radial and vertical mass flux (not shown) of the local environment prior to storm genesis shows strong inward radial mass flux at the surface for CNTL and NightOnly. The strongest vertical mass flux was found near deep moist convection. Minimal low-level convergence and vertical mass flux was observed for DayOnly, with net subsidence from 2 km extending through the tropopause from 1200 UTC 12 September through 0000 UTC 13 September. As expected, the simulations with strong deep moist convection—CNTL and NightOnly—showed stronger low-level convergence and vertical mass flux.

4. Impact of diurnal radiation cycle on local and large-scale environment

Previous studies (Tao et al. 1996; Craig 1996) show that large-scale clear-air cooling impacts storm development, for both MCSs and tropical cyclones. For this study, radiative heating and cooling differences for each sensitivity experiment are hypothesized to impact the local and large-scale environment, altering the evolution of the overall pregenesis environment.

It should be noted that the environment and radiative heating profiles examined herein are clear air only. Clear air is defined as any grid point in the model with a cloud mixing ratio or cloud and ice mixing ratio less than a threshold of $1 \times 10^{-6}\,kg\,kg^{-1}$. The clear-air assumption does not take into account the impact of clouds in the modification of the local and large-scale environment, except implicitly through the detrainment and transport of cloud water.

The impact of diurnal radiation can be seen by examining the 24-h departure of moist static energy (MSE) in the clear-air large-scale environment of each sensitivity experiment from the initial conditions (Fig. 8). MSE is a thermodynamic variable derived from the first law of thermodynamics (Wallace and Hobbs 2006, p. 86) that is approximately conserved following air parcels. It is the sum of the moist enthalpy and gravitational potential energy per unit mass; in other words, it is the total energy content of the air excluding kinetic energy. MSE in a closed system can only be changed by surface fluxes of latent and sensible heat and/or radiative heating. Focusing on DayOnly (Fig. 8b) during the first 24 h, it is clear that the MSE in the PBL is increasing over the initial condition, driven by latent and sensible heat flux. There is a large increase in MSE in the mid- to upper troposphere, caused by shortwave radiative heating of the large-scale environment. NightOnly (Fig. 8c) shows a decrease in MSE above about 3 km extending to the tropopause, driven by the clear-air radiative cooling of the large-scale environment. The MSE panels of Fig. 8 indicate the dominant impact that radiation has on the large-scale mid- to upper-level temperature of the environment. A similar MSE departure was found for the local environment of the clear air (not shown).

To help explain the impact of longwave and shortwave radiation on the large-scale environment, the net (Fig. 9a), shortwave (Fig. 9b), and longwave (Fig. 9c) clear-air and cloudy-air radiative heating tendency profiles are averaged over the first 24 h. The focus is on the large-scale clear-air vertical profiles. The cloudy-air vertical profiles for the large-scale environment and similar net (Fig. 9d),

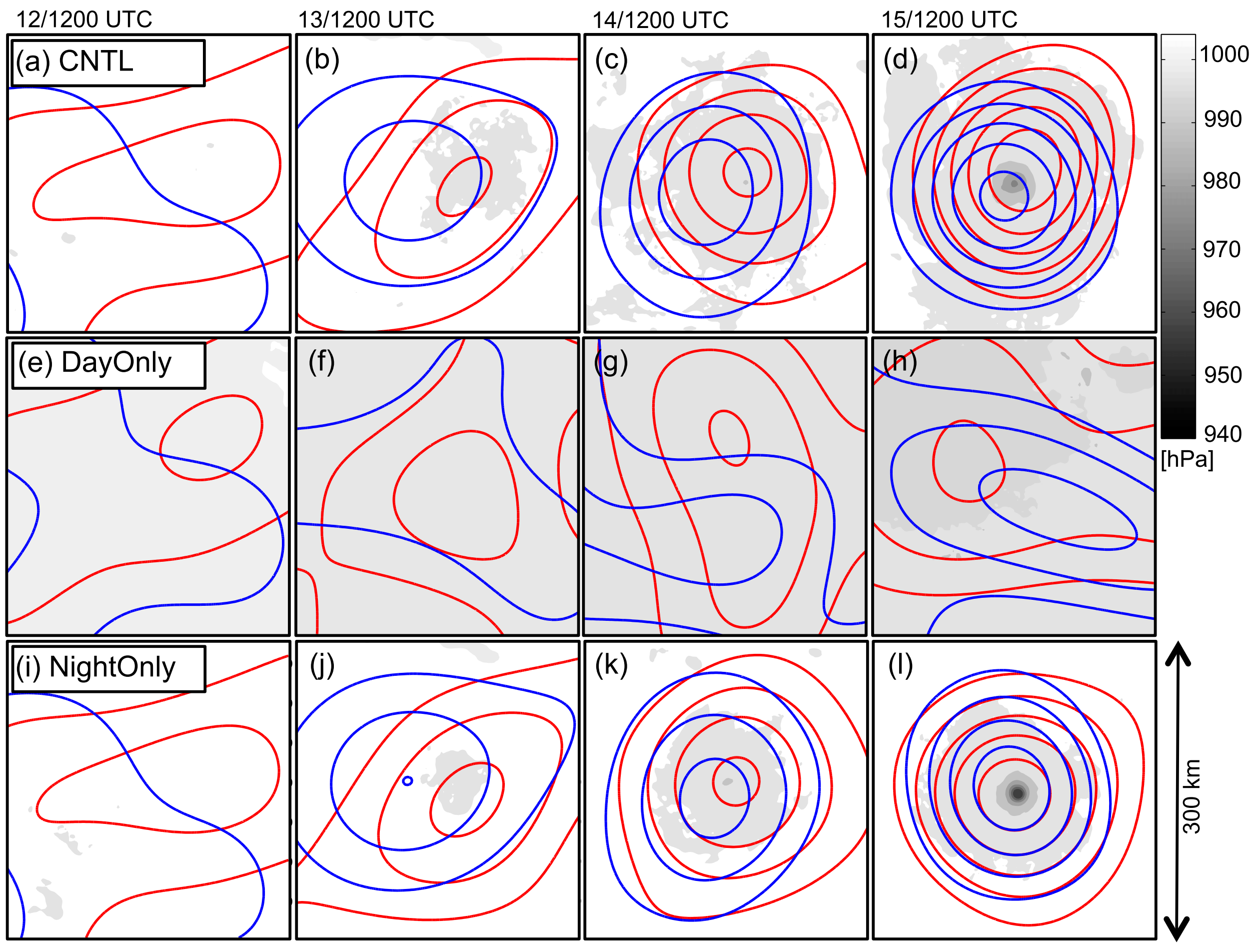

FIG. 7. Filtered relative vorticity (wavelengths less than 300 km removed) contoured every $4 \times 10^{-5}\,\mathrm{s}^{-1}$ (starting at $2 \times 10^{-4}\,\mathrm{s}^{-1}$) at the 850- (red) and 500-hPa (blue) pressure levels for developing member-16 sensitivity experiments (a)–(d) CNTL, (e)–(h) DayOnly, and (i)–(l) NightOnly. Sea level pressure is shaded every 8 hPa starting at 1004 hPa.

shortwave (Fig. 9e) and longwave (Fig. 9f) vertical profiles for the local environment are provided for reference.

The net clear-air large-scale radiative heating profiles (Fig. 9a; solid lines) show an obvious net heating for DayOnly from about 3 km through 12 km with the remaining members having a net cooling above the surface layer (first few model levels) to the tropopause; NightOnly has the largest net cooling. Focusing on the constituents of the net radiative heating tendency—the clear-air longwave and shortwave radiative heating tendencies—over the first 24 h, DayOnly has a positive shortwave (Fig. 9b; solid lines) heating component throughout the entire troposphere, with a peak near 9 km. A local maximum is seen near 600 m at the top of the PBL. CNTL and Offset have similar positive heating profiles but are smaller in magnitude compared to DayOnly. NightOnly and NoRad do not have shortwave heating by experimental design. The clear-air longwave heating tendency profiles (Fig. 9c; solid lines) show DayOnly with the largest magnitude of longwave cooling at all levels below 9 km and NightOnly and CNTL with the smallest longwave cooling; Offset splits the difference, although closer to NightOnly and CNTL. The constant bombardment (non-inclusion) of shortwave radiation is a dominant constituent of the heating (cooling) of the clear-air atmospheric column for DayOnly (NightOnly). The clear air will therefore emit relatively larger (smaller) amounts of longwave radiation.

The net radiative heating tendency summarizes the impact of radiation on the large-scale, clear-air environment. DayOnly has a reduced cooling below about 3 km and net heating from about 3 to 12 km, stabilizing the large-scale clear-air environment. NightOnly has net radiative cooling above the surface layer through the entire troposphere, destabilizing the large-scale clear-air environment. CNTL and Offset have similar profiles as NightOnly but smaller magnitudes. These results are consistent with past studies including Dudhia (1989), Miller and Frank (1993), and Tao et al. (1996).

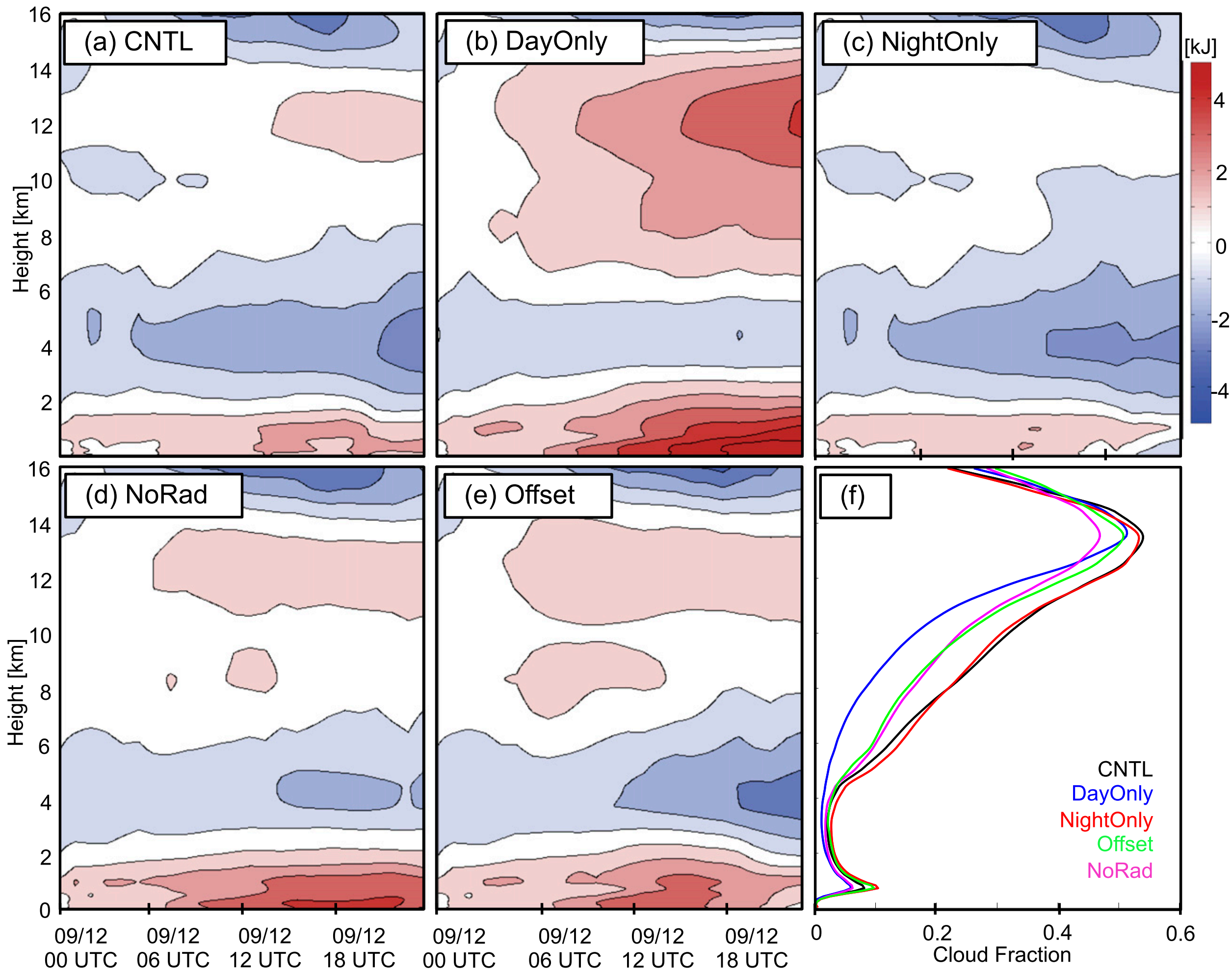

FIG. 8. Vertical profiles of the clear-air large-scale environmental MSE hourly departure (shaded every 1 kJ) from the initial conditions (0000 UTC 12 Sep) for member-16 sensitivity experiment (a) CNTL, (b) DayOnly, (c) NightOnly, (d) NoRad, and (e) Offset. (f) The large-scale cloud fraction is provided for reference for the sensitivity experiments: CNTL (black), DayOnly (blue), NightOnly (red), Offset (green), and NoRad (magenta).

The vertical radiation profiles for the local environment are similar to those of the large scale. The largest differences occur in mid- to upper-tropospheric cloudy air. Comparing Figs. 9c and 9f between 9 and 12 km, there is an increase in the longwave heating for the local environment. This coincides with a 10%–15% (Figs. 8f and 10d) increase in cloud fraction, associated with increased cloud coverage in the local environment. The increased water content produces near-neutral longwave heating for NightOnly and CNTL (Fig. 9f) from 9 to 12 km. The detailed impacts of cloud processes are beyond the scope of this study, but an area of focus for future research.

To study the evolution of the local environment for the first day of the simulation (0000–0000 UTC 12–13 September), vertical profiles of the clear-air 24-h sensitivity experiment departure from CNTL are presented for potential temperature (Fig. 10a), water-vapor mixing ratio (Fig. 10b), and RH (Fig. 10c), with the cloud fraction presented in Fig. 10d. The CNTL 24-h averages for each variable are included for reference.

Figure 10a shows the average potential temperature departure over the first 24 h. Given the net radiative heating tendency profiles described above, it is no surprise that DayOnly (NightOnly) has the highest (lowest) potential temperature throughout the averaged tropospheric profile when compared with CNTL; the remaining members fall in between these bounds. The largest spread lies between the top of the entrainment zone and the tropopause, aligning with vertical layers of net radiative cooling associated with NightOnly and radiative heating associated with DayOnly. The water vapor mixing ratio departure in Fig. 10b is driven by slightly different mechanism, depending

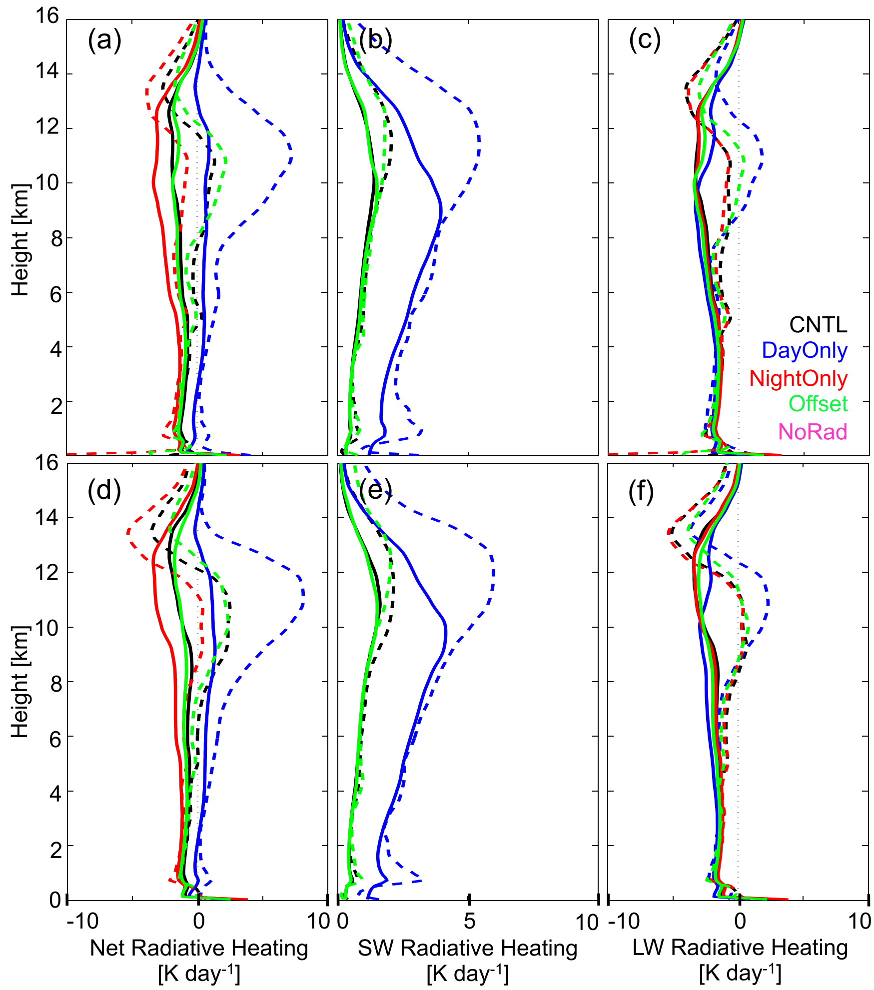

FIG. 9. Clear-air and cloudy-air (a)–(c) large-scale- and (d)–(f) local-environment 0–16-km vertical profiles of (a),(d) net radiative heating (K day^{-1}), (b),(e) shortwave radiative heating (K day^{-1}), and (c),(f) longwave radiative heating (K day^{-1}) averaged over a 24-h period starting at 0000 UTC 12 Sep for member 16. Solid lines are clear-air averages and dashed lines are cloudy-air averages. The sensitivity experiments are colored: CNTL (black), DayOnly (blue), NightOnly (red), Offset (green), and NoRad (magenta).

on the altitude. Below about 1.5 km, the largest departure of water vapor from CNTL is DayOnly, Offset, and NoRad, driven by larger fluxes of water vapor into the mixed layer of the PBL. Aloft, the spread is driven by the increased deep moist convection in NightOnly and NoRad. The impact of the net radiative heating and cooling on the large-scale environment can also be examined by looking at the 24-h-average RH departure profiles in Fig. 10c. Above the PBL, DayOnly has a lower RH, also seen in Fig. 5d. The increase in the potential temperature of DayOnly over the first 24 h above the mixed layer is the dominant mechanism that drives the spread in RH between DayOnly and NightOnly. Tropical environments with larger RH are less detrimental to developing moist convection by diminishing the impact of entrainment. Also, larger RH in the low- to midtroposphere reduces the local stabilization of the PBL by evaporation of precipitation and the transport of low–equivalent potential temperature air toward the surface.

Above the entrainment zone extending to the tropopause, the RH for NightOnly is slightly larger in comparison to CNTL (Fig. 10c). The moister environment in NightOnly is more conducive for deep moist convection relative to CNTL. Although there is no systematic difference between NightOnly and CNTL in the maximum surface (10 m) wind speed (Fig. 3b), the circulation associated with CNTL is not as strong as NightOnly in terms of low- to midlevel vorticity as shown in the Hovmöller diagrams of Fig. 5c versus Fig. 5i, likely as a direct consequence of enhanced convective activity in NightOnly. A

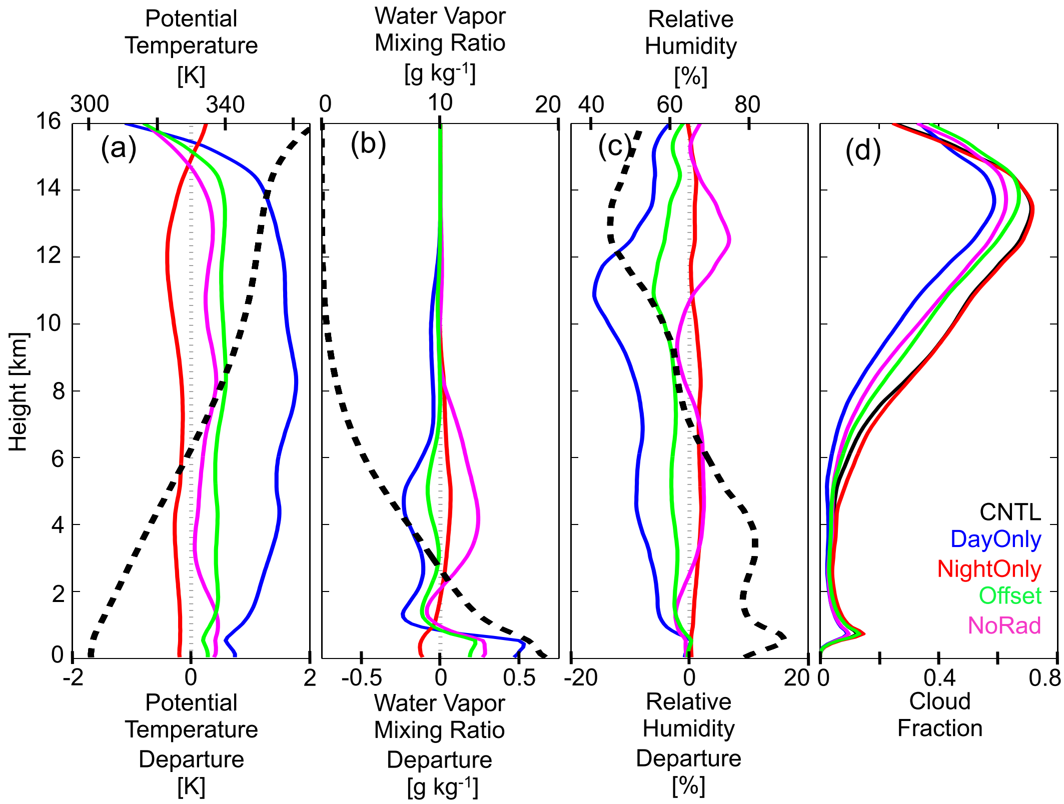

FIG. 10. Clear-air local-environment 24-h-average (starting at 0000 UTC 12 Sep) 0–16-km vertical profiles for CNTL (dashed) and sensitivity experiment departures from CNTL (solid) of (a) potential temperature (K), (b) water vapor mixing ratio ($\mathrm{g\,kg^{-1}}$), and (c) relative humidity (%). (d) The corresponding cloud fraction is also provided. Both sensitivity experiment departures and actual values are colored: CNTL (black), DayOnly (blue), NightOnly (red), Offset (green), and NoRad (magenta).

systematic intensification rate is seen in both Figs. 3b and 3c between NightOnly and CNTL, also seen in Fig. 6 in the average relative vorticity.

To expose why the convection in DayOnly and Offset is suppressed during the first 12 h of the simulation—as seen as a reduction in RH and cloud water and ice in Figs. 5d and 5e for DayOnly—the clear-air local-environment stability above the mixed layer in the entrainment zone is examined. Figure 11 shows a 0–2-km vertical profile of the average local-environment potential temperature (Fig. 11a), saturation equivalent potential temperature θ_e^* (Fig. 11b), RH (Fig. 11c), and water vapor (Fig. 11d). Also shown in Fig. 11 are the 0–2-km vertical profile of the clear-air local average of vertical gradients of potential temperature ($\delta\theta/\delta z$) (Fig. 11e), saturation equivalent potential temperature ($\delta\theta_e^*/\delta z$) (Fig. 11f), temperature ($\delta T/\delta z$) (Fig. 11g), and RH ($\delta\mathrm{RH}/\delta z$) (Fig. 11h). Within the PBL,[3] the local environment is fairly well mixed with gradients in potential temperature, saturation equivalent potential temperature, temperature, and RH fairly uniform, although some deviations between sensitivity experiments exist. The local environmental lapse rate ($\Gamma = -\delta T/\delta z$) is close to dry adiabatic below 200 m and sufficiently mixed up to the top of the PBL where it approaches moist adiabatic (Fig. 11g). The lack of vertical resolution of the model in the PBL is conjectured to be the culprit for a departure from dry adiabatic profiles in the mixed layer.

Focusing on the potential temperature (Fig. 11a), it is clear that DayOnly has the largest value within the PBL and accompanying entrainment zone. The gradient in the potential temperature is a useful diagnostic to determine stability to dry vertical motion. Below 100 m (the first two model levels), $\delta\theta/\delta z < 0$ for all members; the lowest layer of the PBL is absolutely unstable. This is driven by the fixed ocean surface temperature in the model having a temperature slightly above that of the overlying air. Above this shallow layer, the remaining PBL and entrainment zone is stable to dry motions with $\delta\theta/\delta z > 0$ for all sensitivity experiments.

[3] The PBL heights for the sensitivity experiments (not shown) range from 500 to 600 m; NoRad has the largest PBL height followed by DayOnly, Offset, CNTL, and NightOnly. There is a decreasing trend in height for all members throughout the first 24 h.

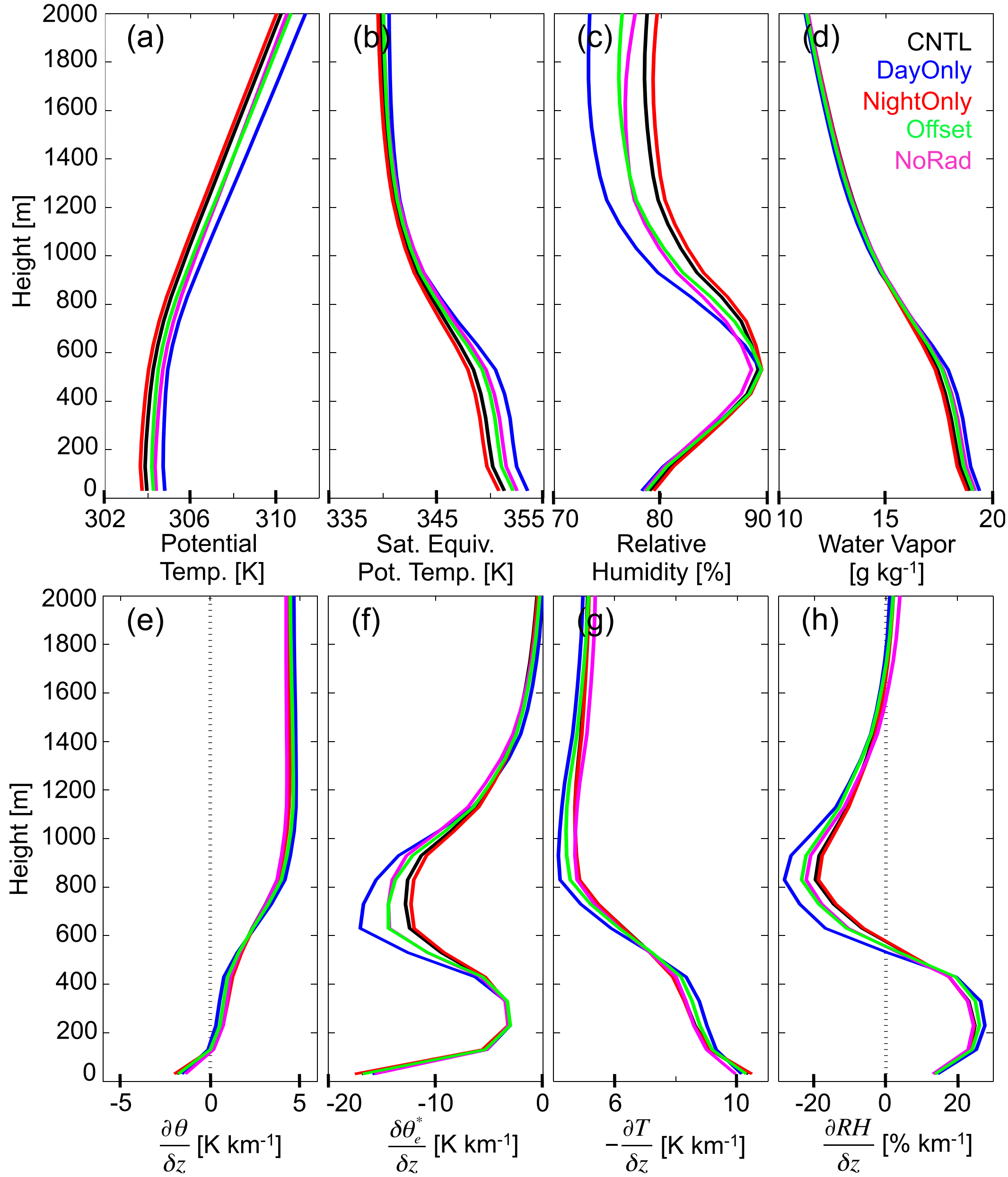

FIG. 11. Clear-air large-scale-environment 0–2-km vertical profiles for (a) potential temperature (K), (b) saturation equivalent potential temperature (K), (c) relative humidity (%), (d) water vapor ($g\,kg^{-1}$), and vertical gradient profiles of the local-environment (e) potential temperature with height ($K\,km^{-1}$), (f) saturation equivalent potential temperature with height ($K\,km^{-1}$), (g) temperature with height ($K\,km^{-1}$), and (h) relative humidity with height ($\%\,km^{-1}$) averaged over a 24-h period starting at 0000 UTC 12 Sep for member 16. The sensitivity experiments are colored: CNTL (black), DayOnly (blue), NightOnly (red), Offset (green), and NoRad (magenta).

Combining the information provided by the gradient of the local-environment saturation equivalent potential temperature (Fig. 11f) and lapse rate (Fig. 11g) and the gradient in potential temperature, discussed above, the environment is found to be conditionally unstable below about 650 m and above about 2000 m with enhanced stability to moist motions in between. The gradient in saturation equivalent potential temperature is negative, $\delta\theta_e^*/\delta z < 0$, for all members, indicating the environment is unstable to moist motions. Above the PBL mixed layer in the entrainment zone, the sensitivity experiments have decreased environmental lapse rates, signifying a relatively stable layer; the local-environment lapse rate of DayOnly and Offset are relatively smaller than that of

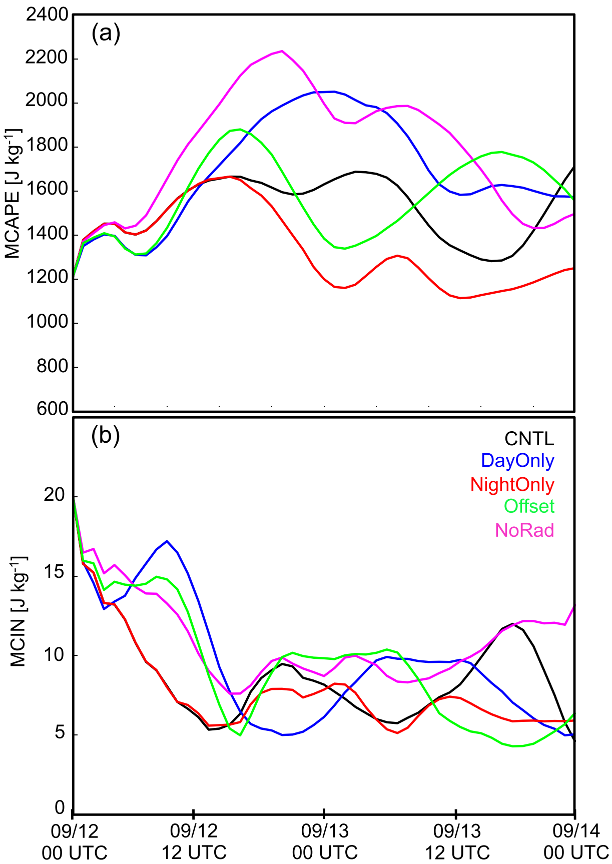

FIG. 12. Clear-air large-scale-environment (a) MCAPE ($J\,kg^{-1}$) and (b) MCIN ($J\,kg^{-1}$) for a parcel (defined as a 500-m-vertical-layer average with the highest equivalent potential temperature below 3000 m AGL) over a 48-h period starting at 0000 UTC 12 Sep for member-16 sensitivity experiments. The sensitivity experiments are colored: CNTL (black), DayOnly (blue), NightOnly (red), Offset (green), and NoRad (magenta).

NightOnly and CNTL, also evident in the large-scale environment, but to a lesser degree.

To assess the impact of the relatively more stable entrainment zone for DayOnly and Offset during the first 12–18 h, the average clear-air large-scale-environment (similar values were derived for the local environment) most unstable convective inhibition (MCIN; Fig. 12b) and most unstable convective available potential energy (MCAPE; Fig. 12a) are plotted for the first 48 h for each sensitivity experiment. The MCAPE and MCIN are for a parcel[4] with the highest equivalent potential temperature below 3000 m AGL. The MCIN for DayOnly, Offset, and NoRad has a relatively larger magnitude than that of NightOnly and CNTL for approximately the first 12–18 h. Focusing on the MCAPE, the instability grows in NoRad and DayOnly after the first 18 h; the increase in MCAPE for DayOnly is a result of the heating and moistening of the DayOnly PBL coupled with the stabilization of the entrainment zone. NoRad is driven by a combination of the heating of the PBL through sensible and latent heat and a lack of heating or cooling in the clear-air large-scale environment. As the simulations progress, NightOnly is continuously convectively active, consuming CAPE and maintaining the low MCAPE values (not shown).

A potential contribution to the stabilization of the entrainment zone is the impact of differential radiative heating and cooling at the RH gradient (Pakula and Stephens 2009; Mapes and Zuidema 1996). Moist air below relatively drier air cools at a larger rate than the drier air above, heating the base of the drier air and thus aiding in the stabilization of that relatively drier layer. This may help to maintain and/or strengthen the stability above the PBL in the entrainment zone. DayOnly has the largest gradient in RH at the entrainment zone (Fig. 11h), with reduced RH above about 2 km. The enhanced mixing in the PBL and an increase in water vapor in DayOnly, Offset, and NoRad provides additional sharpening of the moisture gradient at the top of the mixed layer of the PBL. CNTL and NightOnly have weaker gradients in RH below the entrainment zone. A peak in the longwave radiation tendency near the top of the PBL (~500–650 m) is associated with the moist mixed layer in the PBL environment. There is a local maximum in shortwave heating tendency at the top of the PBL (Fig. 10b) extending into the entrainment zone for DayOnly—around 650 m. The gradient in RH (Fig. 11h) associated with the base of the entrainment zone produces a longwave cooling stratification that may aid in the impact on the local vertical temperature profile of each sensitivity experiment. The net effect of the differential longwave cooling and additional shortwave heating (in experiments with daytime) at and below the entrainment zone is to modify the stability of the entrainment zone, enhancing the stability in DayOnly and to a lesser extent, Offset, relative to that in CNTL and NightOnly. It is obvious that DayOnly has increased stability to moist vertical motions during the initial 12 h, which suppresses convection during the initial 12–18 h of the simulation.

The diurnal radiation cycle impacts the pregenesis local and large-scale environment of Karl by modifying the deep-layer stability and the stability in the entrainment zone, resulting in variations in the amount and timing of deep moist convection during the initial development of the simulation. The relative vorticity, RH, and deep moist convection are coupled, developing sensitivity experiments

[4] A parcel is defined as a 500-m-vertical-layer average at each horizontal grid point.

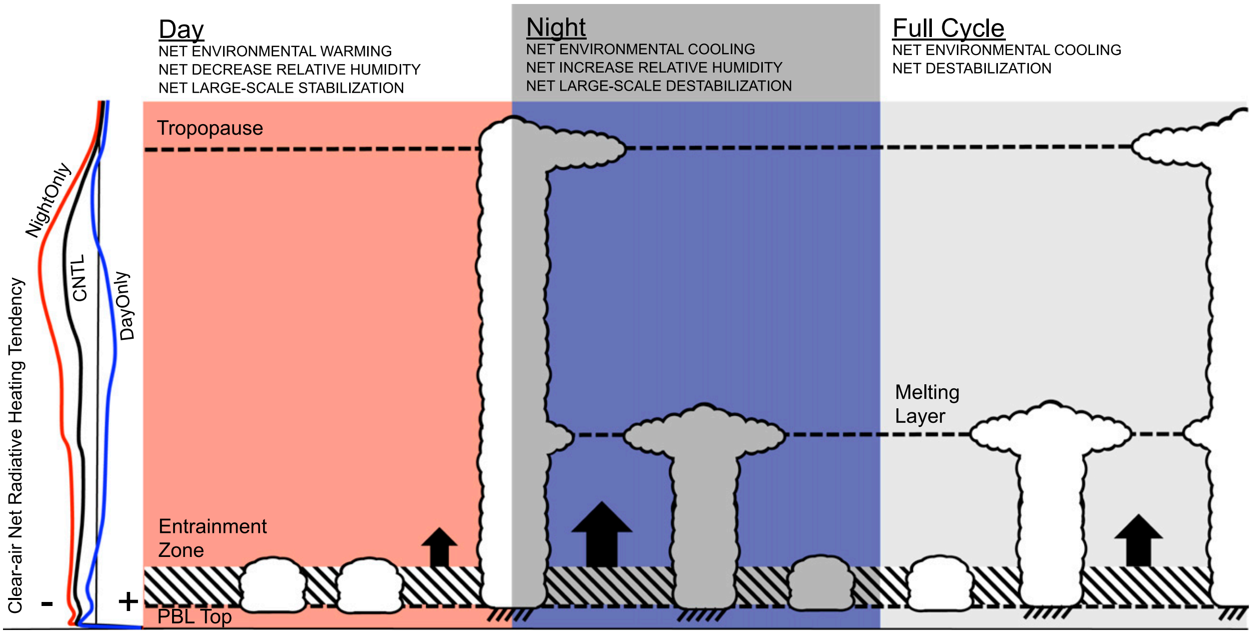

FIG. 13. Schematic depiction of the diurnal radiation cycle impact on the clear-air local and large-scale environment for the genesis of Hurricane Karl during the first 24 h of the simulation. The red (blue) background shading of day (night) indicates net clear-air large-scale environmental heating (cooling). (left) The vertical profile of net clear-air radiation tendency for sensitivity experiments NightOnly (red), DayOnly (blue), and CNTL (black) are depicted for reference. Arrows indicate the local-environment clear-air net radiative cooling (solid) for the entrainment zone; the size indicates relative magnitude. The schematic is drawn to scale. During the nighttime, net cooling of the clear-air large-scale environment from longwave emission reduces static stability with a corresponding net increase in relative humidity. A large net cooling of the entrainment zone reduces stability of the low-level entrainment stable layer in the local environment. The combined impact is an overall environment more conducive for vigorous deep moist convection. During the daytime, the clear-air large-scale environmental heating from shortwave radiation is larger in magnitude than the cooling from longwave radiation above about 3 km, causing a net stabilization of the clear-air large-scale environment. Within the entrainment zone, a relatively smaller net cooling occurs because of the combined effect of shortwave radiation from above and increased longwave radiative emission from the relatively moist PBL below. The increased stability of the entrainment stable layer and stabilization of the local environment leads to the suppression of convective activity during the first 12–18 h of the simulation, altering the subsequent evolution of tropical cyclone development. Note that the cloud distributions and stable layers for the first 12–18 h are shown for reference. Schematic adapted from Johnson et al. (1999), first documented by Malkus (1956).

CNTL, NightOnly, and Offset have a period of strong deep moist convection during the second half of the first 24 h. The associated burst of deep moist convection is hypothesized to be the catalyst driving the increased relative vorticity at the surface and midlevels (Figs. 5c,i) and moistening of the low- and midlevels (Figs. 5a,c) that leads to the eventual development of the tropical cyclone. Our finding is consistent with DA12, who observed the relationship between deep moist convection modulated by a strong diurnal cycle and the intensification of the pregenesis circulation of Karl.

A schematic depiction of the diurnal radiation cycle impacts is shown in Fig. 13, displaying the NightOnly and DayOnly radiative differences of the combined local and large-scale environment and stable layers; CNTL is provided for reference. During nighttime, the net cooling of the clear-air local and large-scale environment from longwave emission reduces static stability with a corresponding net increase in RH; the overall environment is more conducive to vigorous convection that precedes the genesis of Karl. During the daytime, the heating from shortwave radiation is larger in magnitude than the cooling from longwave radiation in the mid- to upper-level clear-air local and large-scale environment, leading to a net stabilization. An enhancement in stability of the entrainment zone (due to the shortwave radiative heating and the differential radiative heating of the relatively drier air at the interface between the top of the PBL and the entrainment zone) produces a smaller cooling rate in the entrainment zone, leading to increased stability and an initial period of suppressed convective activity in the local environment. For the full diurnal cycle (CNTL), the shortwave heating of the local and large-scale environment offsets a portion of the cooling seen in the nighttime-only experiment throughout the troposphere, producing a relatively closer to neutral cooling vertical profile, but still providing net destabilization.

5. Concluding remarks

This study examined the effect of the diurnal radiation cycle on the pregenesis environment of Hurricane Karl (2010). The sensitivity experiments are intended to isolate various parts of the diurnal radiation cycle, which include endless daytime, endless nighttime, no radiation, a normal diurnal cycle, and a reversal of the diurnal cycle that shifts the model time backward by 12 h. The initial conditions were taken from a 30-member ensemble analysis generated during the PREDICT field campaign from the cycling PSU WRF-EnKF system; two developing and two nondeveloping ensemble members were chosen for the sensitivity experiments.

Potential tropical cyclogenesis was found to be sensitive to the heating and cooling associated with the diurnal cycle and its impact on deep moist convection. The nighttime phase of the diurnal radiation cycle provides critical destabilization in the pregenesis local and large-scale clear-air environment, promoting deep moist convection and increased relative humidity throughout the troposphere, thus improving chances for cyclogenesis. The daytime phase of the diurnal radiation cycle is critical in reducing the local and large-scale relative humidity and increasing the stability, making the overall environment less conducive to deep moist convection and thus altering the local environmental evolution and subsequent tropical cyclone development. The impact of radiation was found to be an integrated effect, taking time ($\sim$10 h) for the radiation scheme modifications to noticeably alter the local and large-scale environment.

Relative humidity gradients at the base of dry layers in the troposphere can provide a region of anomalous longwave radiative heating and stabilization at the base of the dry layer and a layer of anomalous longwave radiative cooling of the moist layer below. This is hypothesized to play a role in enhancing the stability associated with the entrainment zone in this study. During the initial period, DayOnly and Offset sensitivity experiments produce larger relative humidity gradients at the top of the PBL, driven by increased boundary layer mixing from absorption of shortwave radiation in DayOnly and Offset. Note that the sea surface temperature is fixed. NightOnly and CNTL experiments have reduced relative humidity gradients because of reduced heating and moistening of the PBL. The stability within the entrainment zone above the PBL top is crucial to the development of deep moist convection during the first 12–18 h. Experiments with only the daytime phase have enhanced stability from additional shortwave heating of the entrainment zone, increasing the convective inhibition and preventing moist convection during the initial 12–18 h. The daytime phase of the diurnal cycle is conjectured to play a role in stabilizing the entrainment zone. Experiments including a nighttime phase of the diurnal cycle have reduced stability of the entrainment zone and reduced convective inhibition, enhancing the development potential of deep moist convection.

The analysis of sensitivity experiments performed on two original developing ensemble members found that radiation may impact the rate of intensification, but no discernable difference in timing of intensification was discovered. The nighttime-only simulations, with only longwave cooling, were more intense by the end of the 120-h simulation period and intensified the quickest compared with the simulations that included shortwave radiation. The simulations were not run to a steady state; therefore, the impact on final intensity could not be determined.

The findings herein are preliminary and the robustness of the results need to be verified with additional case studies. This study focused on one cyclogenesis case—one tropical cyclone basin—and emphasis was placed on the first 24 h of the model simulations. Only one PBL scheme is used in the construction of the experiment and the robustness of the results to different PBL schemes is not examined. The YSU PBL scheme explicitly models entrainment in the entrainment zone; this may have an impact on the stability of the entrainment zone and deep moist convective development. Future work is needed to stress test these results using different pairings of PBL schemes, radiation schemes, and microphysics schemes available in WRF.

Acknowledgments. The authors thank Dr. Yonghui Weng for performing the real-time ensemble data assimilation and forecasts that are used in this study and Dr. Xiaqiong Zhou for initiating some of preliminary analysis of the diurnal cycle and sensitivity. This research was partially supported by ONR (Grant N000140910526), NOAA (HFIP), NASA (NNX12AJ79G), and the NSF (Grant 0840651). The computing is primarily conducted at the Texas Advanced Computing Center (TACC) and the Jet supercomputer cluster at NOAA's Earth System Research Laboratory.

REFERENCES

Baik, J.-J., M. DeMaria, and S. Raman, 1990: Tropical cyclone simulations with the Betts convective adjustment scheme. Part II: Sensitivity experiments. *Mon. Wea. Rev.,* **118,** 529–541, doi:10.1175/1520-0493(1990)118<0529:TCSWTB>2.0.CO;2.

Barker, D. M., W. Huang, Y.-R. Guo, A. J. Bourgeois, and Q. N. Xiao, 2004: A three-dimensional variational data assimilation system for MM5: Implementation and initial results. *Mon. Wea. Rev.,* **132,** 897–914, doi:10.1175/1520-0493(2004)132<0897:ATVDAS>2.0.CO;2.

Craig, G., 1996: Numerical experiments on radiation and tropical cyclones. *Quart. J. Roy. Meteor. Soc.,* **122,** 415–422, doi:10.1002/qj.49712253006.

Davis, C. A., and D. A. Ahijevych, 2012: Mesoscale structural evolution of three tropical weather systems observed during PREDICT. *J. Atmos. Sci.,* **69,** 1284–1305, doi:10.1175/JAS-D-11-0225.1.

Dudhia, J., 1989: Numerical study of convection observed during the Winter Monsoon Experiment using a mesoscale two-dimensional model. *J. Atmos. Sci.,* **46,** 3077–3107, doi:10.1175/1520-0469(1989)046<3077:NSOCOD>2.0.CO;2.

Fovell, R. G., K. L. Corbosiero, A. Seifert, and K.-N. Liou, 2010: Impact of cloud-radiative processes on hurricane track. *Geophys. Res. Lett.,* **37,** L07808, doi:10.1029/2010GL042691.

Grell, G., and D. Devenyi, 2002: A generalized approach to parameterizing convection combining ensemble and data assimilation techniques. *Geophys. Res. Lett.,* **29,** doi:10.1029/2002GL015311.

Hack, J. J., 1980: The role of convective-scale processes in tropical cyclone development. Ph.D. dissertation, Colorado State University, 206 pp.

Hong, S., and J. J. Lim, 2006: The WRF single-moment 6-class microphysics scheme (WSM6). *J. Korean Meteor. Soc.,* **42,** 129–151.

——, Y. Noh, and J. B. Dudhia, 2006: A new vertical diffusion package with an explicit treatment of entrainment processes. *Mon. Wea. Rev.,* **134,** 2318–2341, doi:10.1175/MWR3199.1.

Johnson, R., P. Ciesielski, and K. Hart, 1996: Tropical inversions near the 0°C level. *J. Atmos. Sci.,* **53,** 1838–1855, doi:10.1175/1520-0469(1996)053<1838:TINTL>2.0.CO;2.

——, T. Rickenbach, S. Rudledge, P. Ciesielske, and W. Schubert, 1999: Trimodal characteristics of tropical convection. *J. Climate,* **12,** 2397–2418, doi:10.1175/1520-0442(1999)012<2397:TCOTC>2.0.CO;2.

Kossin, J. P., 2002: Daily hurricane variability inferred from GOES infrared imagery. *Mon. Wea. Rev.,* **130,** 2260–2270, doi:10.1175/1520-0493(2002)130<2260:DHVIFG>2.0.CO;2.

Malkus, J. S., 1956: On the maintenance of the trade winds. *Tellus,* **8,** 335–350, doi:10.1111/j.2153-3490.1956.tb01231.x.

Mapes, B. E, and P. Zuidema, 1996: Radiative-dynamical consequences of dry tongues in the tropical atmosphere. *J. Atmos. Sci.,* **53,** 620–638, doi:10.1175/1520-0469(1996)053<0620:RDCODT>2.0.CO;2.

McBride, J. L., and R. Zehr, 1981: Observational analysis of tropical cyclone formation. Part II: Comparison of non-developing versus developing systems. *J. Atmos. Sci.,* **38,** 1132–1151, doi:10.1175/1520-0469(1981)038<1132:OAOTCF>2.0.CO;2.

Meng, Z., and F. Zhang, 2008a: Tests of an ensemble Kalman filter for mesoscale and regional-scale data assimilation. Part III: Comparison with 3DVAR in a real-data case study. *Mon. Wea. Rev.,* **136,** 522–540, doi:10.1175/2007MWR2106.1.

——, and ——, 2008b: Tests of an ensemble Kalman filter for mesoscale and regional-scale data assimilation. Part IV: Comparison with 3DVAR in a month-long experiment. *Mon. Wea. Rev.,* **136,** 3671–3682, doi:10.1175/2008MWR2270.1.

Miller, R. A., and W. M. Frank, 1993: Radiative forcing of simulated tropical cloud clusters. *Mon. Wea. Rev.,* **121,** 482–498, doi:10.1175/1520-0493(1993)121<0482:RFOSTC>2.0.CO;2.

Mlawer, E. J., S. J. Taubman, P. D. Brown, M. J. Iacono, and S. A. Clough, 1997: Radiative transfer for inhomogeneous atmosphere: RRTM, a validated correlated-k model for the long-wave. *J. Geophys. Res.,* **102** (D14), 16 663–16 682, doi:10.1029/97JD00237.

Montgomery, M. T., and Coauthors, 2012: The Pre-Depression Investigation of Cloud-Systems in the Tropics (PREDICT) experiment: Scientific basis, new analysis tools, and some first results. *Bull. Amer. Meteor. Soc.,* **93,** 153–172, doi:10.1175/BAMS-D-11-00046.1.

Munsell, E. B., F. Zhang, and D. P. Stern, 2013: Predictability and dynamics of a non-intensifying tropical storm: Erika (2009). *J. Atmos. Sci.,* **70,** 2505–2524, doi:10.1175/JAS-D-12-0243.1.

Pakula, L., and G. L. Stephens, 2009: The role of radiation in influencing tropical cloud distributions in a radiative–convective equilibrium cloud-resolving model. *J. Atmos. Sci.,* **66,** 62–76, doi:10.1175/2008JAS2738.1.

Posselt, D. J., S. C. van den Heever, and G. L. Stephens, 2008: Trimodal cloudiness and tropical stable layers in simulations of radiative–convective equilibrium. *Geophys. Res. Lett.,* **35,** L08802, doi:10.1029/2007GL033029.

Poterjoy, J., and F. Zhang, 2014: Predictability and genesis of Hurricane Karl (2010) examined through the EnKF assimilation of field observations collected during PREDICT. *J. Atmos. Sci.,* doi:10.1175/JAS-D-13-0291.1, in press.

Sippel, J. A., and F. Zhang, 2008: A probabilistic analysis of the dynamics and predictability of tropical cyclogenesis. *J. Atmos. Sci.,* **65,** 3440–3459, doi:10.1175/2008JAS2597.1.

——, and ——, 2010: Factors affecting the predictability of Hurricane Humberto (2007). *J. Atmos. Sci.,* **67,** 1759–1778, doi:10.1175/2010JAS3172.1.

Skamarock, W. C., and Coauthors, 2008: A description of the Advanced Research WRF version 3. NCAR Tech. Note NCAR/TN-475+ STR, 113.

Stephens, G. L., 1978a: Radiation profiles in extended water clouds. I: Theory. *J. Atmos. Sci.,* **35,** 2111–2122, doi:10.1175/1520-0469(1978)035<2111:RPIEWC>2.0.CO;2.

——, 1978b: Radiation profiles in extended water clouds. II: Parameterization schemes. *J. Atmos. Sci.,* **35,** 2123–2132, doi:10.1175/1520-0469(1978)035<2123:RPIEWC>2.0.CO;2.

Steranka, J., E. B. Rodgers, and R. C. Gentry, 1984: The diurnal variation of Atlantic Ocean tropical cyclone cloud distribution inferred from geostationary satellite infrared measurements. *Mon. Wea. Rev.,* **112,** 2338–2344, doi:10.1175/1520-0493(1984)112<2338:TDVOAO>2.0.CO;2.

Stewart, S. R., 2010: Tropical cyclone report Hurricane Karl (AL1312010) 14-18 September 2010. National Hurricane Center Tech. Rep., 17 pp. [Available online at http://www.nhc.noaa.gov/pdf/TCR-AL132010_Karl.pdf.]

Sundqvist, H., 1970: Numerical simulation of the development of tropical cyclones with a ten-level model. Part II. *Tellus,* **22,** 504–510, doi:10.1111/j.2153-3490.1970.tb00516.x.

Tao, W.-K., S. Lang, J. Simpson, C.-H. Sui, B. Ferrier, and M.-D. Chou, 1996: Mechanisms of cloud-radiation interaction in the tropics and midlatitudes. *J. Atmos. Sci.,* **53,** 2624–2651, doi:10.1175/1520-0469(1996)053<2624:MOCRII>2.0.CO;2.

Torn, R. D., and D. Cook, 2013: The role of vortex and environment errors in genesis forecasts of Hurricanes Danielle and Karl (2010). *Mon. Wea. Rev.,* **141,** 232–251.

Wallace, J. M., and P. V. Hobbs, 2006: *Atmospheric Science: An Introductory Survey.* 2nd ed. Academic Press, 504 pp.

Weng, Y., and F. Zhang, 2012: Assimilating airborne Doppler radar observations with an ensemble Kalman filter for convection-permitting hurricane initialization and prediction: Katrina (2005). *Mon. Wea. Rev.,* **140,** 841–859, doi:10.1175/2011MWR3602.1.

Zhang, F., and J. A. Sippel, 2009: Effects of moist convection on hurricane predictability. *J. Atmos. Sci.,* **66,** 1944–1961, doi:10.1175/2009JAS2824.1.

——, Y. Weng, J. A. Sippel, Z. Meng, and C. H. Bishop, 2009: Cloud-resolving hurricane initialization and prediction through assimilation of Doppler radar observations with an ensemble Kalman filter. *Mon. Wea. Rev.,* **137,** 2105–2125, doi:10.1175/2009MWR2645.1.

——, ——, J. F. Gamache, and F. D. Marks, 2011: Performance of convection-permitting hurricane initialization and prediction during 2008–2010 with ensemble data assimilation of inner-core airborne Doppler radar observations. *Geophys. Res. Lett.,* **38,** L15810, doi:10.1029/2011GL048469.